




Chemical Evolution During the Formation of Molecular Clouds

Jingfei Sun^{1,2} and Fujun Du^{1,2} 

¹ Purple Mountain Observatory, Chinese Academy of Sciences, Nanjing 210023, China; fjdu@pmo.ac.cn

² School of Astronomy and Space Science, University of Science and Technology of China, Hefei 230026, China

Received 2022 February 9; revised 2022 April 9; accepted 2022 April 27; published 2022 June 6

Abstract

To study the chemical evolution during the formation of molecular clouds, we model three types of clouds with different density structures: collapsing spherical, collapsing ellipsoidal, and static spherical profiles. The collapsing models are better than the static models in matching the observational characteristics in typical molecular clouds. This is mainly because the gravity can speed up the formation of some important molecules (e.g., H₂, CO, OH) by increasing the number density during collapse. The different morphologies of prolate, oblate, and spherical clouds lead to differences in chemical evolution, which are mainly due to their different evolution of number density. We also study the effect of initial chemical compositions on chemical evolution, and find that H atoms can accelerate OH formation by two major reactions: O + H → OH in gas phase and on dust grain surfaces, leading to the models in which hydrogen is mainly atomic initially better match observations than the models in which hydrogen is mainly molecular initially. Namely, to match observations, initially hydrogen must be mostly atomic. The CO molecules are able to form even without the pre-existence of H₂. We also study the influence of gas temperature, dust temperature, intensity of interstellar radiation field and cosmic-ray ionization rate on chemical evolution in static clouds. The static CO clouds with high dust temperature, strong radiation field, and intensive cosmic rays are transient due to rapid CO destruction.

Key words: ISM: abundances – (ISM:) evolution – ISM: molecules

1. Introduction

It is known that atomic hydrogen can be converted into molecular hydrogen when dust grains or electrons act as a catalyst (McCrea & McNally 1960; McDowell 1961). Almost all H₂ form on dust grain surfaces in the local universe where the metallicity is relatively high (Ballesteros-Paredes et al. 2020). It is not yet clear how diffuse atomic gas turns into dense molecular gas in the Milky Way. The primary mechanisms of molecular cloud formation which have been proposed are thermal instabilities (Field 1965), converging flows (Bania & Lyon 1980), stellar feedback processes such as the expansion of H II regions and supernova blast wave, cloud–cloud collisions (Oort 1954; Field & Saslaw 1965), agglomeration of smaller clouds (Casoli & Combes 1982), gravitational instabilities (Goldreich & Lynden-Bell 1965), magnetic instabilities (Parker 1966) and magneto-rotational instabilities (Balbus & Hawley 1991). Both observations and theories show the properties of molecular clouds depend on the galactic environment, so different mechanisms of molecular cloud formation may dominate different clouds.

There are two distinct chemical phases in the neutral clouds: atomic and molecular. The atomic phase mainly consisted of neutral atomic hydrogen (HI) can be traced by the HI hyperfine transition at $\lambda = 21$ cm. Since the first detection of the 21 cm line by the Harvard team in 1951

(Ewen & Purcell 1951), there have been more and more studies on atomic hydrogen. Li & Goldsmith (2003) and Goldsmith & Li (2005) used the HI narrow self-absorption (HINSA) technique to study atomic hydrogen in dark clouds. Furthermore, the transition from atomic to molecular hydrogen in dense clouds was studied by modeling the HINSA feature from cold atomic hydrogen (Goldsmith et al. 2007). Numerous HI self-absorption observations (e.g., Bigiel et al. 2008; Barriault et al. 2010; Stanimirović et al. 2014; Burkhart et al. 2015) indicate an upper column density threshold of $\sim 10^{21}$ cm⁻² for cold HI in molecular clouds, consistent with semi-analytical models (Sternberg et al. 2014; Bialy & Sternberg 2016). The hydrogen molecule is non-polar and lacks a permanent electric dipole moment, hence it can only radiate through rovibrational or very weak quadrupole and induced dipole rotational transitions (Field et al. 1966). Furthermore, the vibrational ground state with rotation level $J = 2$ is 512 K above $J = 0$ and requires a temperature of hundreds of Kelvin to excite. These are reasons why the direct detection of H₂ is difficult by the emission of H₂ in cold interstellar medium. The molecular phase is primarily traced by other molecular species, and one of the most common molecules to trace H₂ is the CO molecule, but CO as a tracer also has its shortcomings, one being that CO cannot trace all the H₂ gas.

The existence of molecular gas that cannot be traced by CO (CO-dark molecular gas) has been known for many years (Lada & Blitz 1988). Tielens & Hollenbach (1985) predicted the existence of H₂ and C⁺ layers from theoretical models of molecular clouds. At the same time, various observations also indicate the existence of CO-dark molecular gas (Reach et al. 1994; Grenier et al. 2005; Langer et al. 2010, 2014; Planck Collaboration et al. 2011; Pineda et al. 2013). It has been explored whether OH clouds serve as a more effective tracer of CO-dark molecular gas (Li et al. 2015), so OH molecule is critical for studying interstellar medium.

There have been many observations of CO and OH molecules in molecular clouds. Sofia et al. (2004) acquired a CO abundance of $\sim 3.2 \times 10^{-4}$ toward some translucent sight lines in the galaxy. In some CO-poor clouds, the CO abundance can be even lower than $\sim 2.1 \times 10^{-6}$ (Tang et al. 2017). These observations suggest there is a great difference in the CO abundance for different clouds. Both radio and UV observations suggest that OH abundance is in a wide range. Crutcher (1979) reviewed the data for diffuse clouds and concluded an OH abundance of 5×10^{-8} . The OH abundance is close to 2×10^{-8} by observations for a sample of compact extragalactic mm-wave continuum sources (Liszt & Lucas 1996). Weselak et al. (2010) detected OH molecule toward 16 translucent sight lines and obtained an average OH abundance of 1.05×10^{-7} . The OH abundance in molecular clouds ranges from 5.7×10^{-8} to 4.8×10^{-6} (Tang et al. 2021).

In this work we explore to what extent can we use chemical modeling to constrain their formation and early stages of clouds. We use Chempl in this work, and we adopt a large reaction network. We focus on the importance of some physical parameters for chemical models. We model three types of density structures: gravitationally collapsing uniform spherical and ellipsoidal (prolate and oblate), and static spherical profiles.

This paper is organized as follows. In Section 2, we briefly describe the Chempl code. Section 3 shows three types of density profiles, physical parameters, and initial abundances used in our models. In Section 4, we present chemical evolution of four species (H, H₂, CO, and OH) in these clouds. Section 5 shows the influence of the gas temperature (T_{gas}), the dust temperature (T_{dust}), the intensity of interstellar radiation field (G_0 , the ratio between the actual radiation field and Draine 1978 interstellar field), and cosmic-ray ionization rate (ζ , H₂ ionization per sec) on abundances for these four species. In Section 6, we discuss the influence of initial abundances, density profiles, and physical parameters on the evolution of clouds. Conclusions are presented in Section 7. The Appendix gives additional figures related to the main part of this work.

2. Methodology

There are a few codes for chemical modeling, e.g., Nahoon (Wakelam et al. 2012), MAGICCAL (Garrod 2013), KROME

Table 1
Some Physical Parameters and their Typical Values Used in Models

G_0	1
T_{dust}	15 K
T_{gas}	30 K
ζ	$3 \times 10^{-17} \text{ s}^{-1}$
Dust-to-gas mass ratio	0.01
Dust albedo	0.6
Dust grain radius	0.1 μm
Dust material density	2.0 g cm^{-3}
Dust site density	10^{15} cm^{-2}
Chemical desorption efficiency	0.05
Mean molecular weight	1.4

(Grassi et al. 2014), Astrochem (Maret & Bergin 2015), Nautilus (Ruaud et al. 2016), UCLCHEM (Holdship et al. 2017), and Chempl (Du 2021). The 1D and 2D models in this paper are carried out using the Chempl code (Du 2021), which works with comprehensive gas-grain chemical networks. It supports the three-phase (gas, dust grain surface and mantle) formulation of interstellar gas-grain chemistry. For the current work the UMIST 2012 network (McElroy et al. 2013) is used, augmented by grain surface reactions. In total the network contains 7721 reactions between 703 species.

Chemical modeling requires a lot of physical parameters, but here we only focus on a few physical parameters that are most relevant for chemical reaction rates. Some important physical parameters used in models are listed in Table 1. At present the temperature profiles are input by hand instead of from self-consistent calculation based on cooling and heating balance. It is necessary to provide a suitable value of ζ and G_0 for the models, because the destruction rates of most molecules are greatly affected by cosmic rays and ultra-violet (UV) photons. The cosmic-ray ionization rate is taken to be a constant for simplicity, because it is only weakly attenuated in high column density regions (Padovani et al. 2018). We adopt a common value of ζ and G_0 in Table 1 for the majority of this paper, but also consider the influence of different values of ζ and G_0 on some chemical compositions in Section 5. The shielding effects of H₂ and CO greatly influence the chemical evolution of molecular clouds, so we take the self- and mutual-shielding of H₂ and CO molecules into account. The self-shielding of H₂ from photodissociation is treated using the approach of Draine & Bertoldi (1996), while the shielding of CO is implemented based on Morris & Jura (1983).

3. Density Distribution and Initial Conditions

The gas density is a critical parameter for chemical evolution. In this work we adopt three types of density profiles to study their differences in chemical evolution. While the actual dynamic evolution may not follow a simple process

described by analytical formulas, some qualitative insights can be gained through such a study.

3.1. The Gravitationally Collapsing Uniform Spherical Cloud

Here we consider an isolated spherical cloud with uniform density under self-gravity, neglecting any rotation or magnetic field. The cloud collapses toward the center under self-gravity, through a series of spherically symmetric states. For its mathematical description, we follow the formulation of Lin et al. (1965). To maintain both the spherical shape and uniform density during the collapse, a particle with coordinates (x_0, y_0, z_0) at time $t=0$ must subsequently be at (x, y, z) with

$$x = x_0 X(t), \quad y = y_0 Y(t), \quad z = z_0 Z(t), \quad (1)$$

where $X(t)$, $Y(t)$, $Z(t)$ are dimensionless lengths, and the uniform number density is given by

$$n(t) = \frac{n_0}{X(t)Y(t)Z(t)}, \quad (2)$$

where n_0 is the initial number density.

For the spherical case, we use spherical coordinates (r, θ, φ) , and then give the uniform number density:

$$n = \frac{n_0}{R^3(t)}, \quad (3)$$

where the dimensionless radius is defined by $R(t) \equiv r/r_0$, and r_0 is initial radius. The time evolution of a spherical cloud is given by Lin et al. (1965)

$$R = \cos^2 \delta, \quad \tau = \left(\frac{8\pi}{3}\right)^{-\frac{1}{2}} \left(\delta + \frac{1}{2} \sin 2\delta\right), \quad \tau \equiv (G\rho_0)^{\frac{1}{2}} t, \quad (4)$$

where τ is a dimensionless time (note that $(G\rho_0)^{1/2}$ is within one order of magnitude of the inverse of freefall timescale), G is the gravitational constant, ρ_0 is the initial mass density, and δ is an implicit function of time, which is needed to numerically calculate the evolution of density as a function of time. From Equations (3)–(4), we get

$$n(t) = \frac{n_0}{(\cos \delta(t))^6}. \quad (5)$$

3.2. The Gravitationally Collapsing Uniform Ellipsoidal Cloud

Next, we consider the cases of uniform oblate and prolate spheroids, using the formula of Lin et al. (1965). For the spheroidal cases, we use cylindrical coordinates (r, θ, z) , and the uniform number density is

$$n = \frac{n_0}{R^2(t)Z(t)}, \quad (6)$$

where the dimensionless radius is defined by $R(t) \equiv r/r_0$, r_0 is initial radius, the dimensionless height is defined by $Z(t) \equiv z/z_0$, and z_0 is initial height.

The time evolution of an oblate ellipsoidal cloud is given by Lin et al. (1965)

$$\begin{aligned} E &= 1 + E_2(\tan \delta)^2 + E_4(\tan \delta)^4, \\ a_0 \tau &= \left(\delta + \frac{1}{2} \sin 2\delta\right) - \left(\frac{a_2}{a_0}\right) \left(\delta - \frac{1}{2} \sin 2\delta\right), \\ R &= \cos^2 \delta, \quad Z = ER, \end{aligned} \quad (7)$$

where E_2, E_4, a_0, a_2 are constants depending on the ellipticity, the dimensionless time τ is defined by Equation (4), and δ is an implicit function of time. From Equations (6)–(7), we get

$$n(t) = \frac{n_0}{E(\cos \delta(t))^6}. \quad (8)$$

Similarly, the time evolution of a prolate ellipsoidal cloud is obtained by Lin et al. (1965)

$$\begin{aligned} E &= 1 + E_2(\tan \delta)^2 + E_4(\tan \delta)^4, \\ a_0 \tau &= \left(\delta + \frac{1}{2} \sin 2\delta\right) - \left(\frac{a_2}{a_0}\right) \left(\delta - \frac{1}{2} \sin 2\delta\right), \\ Z &= \cos^2 \delta, \quad R = EZ. \end{aligned} \quad (9)$$

Then, we get the number density vary with time as

$$n(t) = \frac{n_0}{E^2(\cos \delta(t))^6}. \quad (10)$$

Note that the first two expressions in Equations (7) and (9) are just the first few terms of a series expansion instead of the exact solution. For a specific shape and time, we can calculate the value of δ and E , and then acquire the number density for an ellipsoidal cloud. Here the collapse timescale is defined as the time when the semiminor axis of an ellipsoid shrinks to zero, which is used as the cloud evolution time. The value of E is zero at the time, so we can get the collapse timescale by the value of δ . When the ellipticity of an ellipsoid is close to zero, its collapse timescale becomes the same as the freefall timescale for the spherical case.

To see the differences in the number density between different collapsing models (sphere, oblate ellipsoid, and prolate ellipsoid) with identical initial number density ($n_0 = 50 \text{ cm}^{-3}$), we show the number density as a function of time in Figure 1 (initial shape and number density are introduced in Section 4). When these semiminor axes of collapsing clouds shrink to typical scales of molecular clouds (1–3 pc), we artificially cease their dynamical evolutions, then obtain their end time points. Note the prolate ellipsoid is larger than the oblate ellipsoid initially (given in Section 4), so we adopt a large final scale for the prolate one. The collapse of the sphere is slower than the oblate or prolate spheroid, so morphological anisotropy can lead to large differences in the evolution of number density. At late stages, the shrinkage of

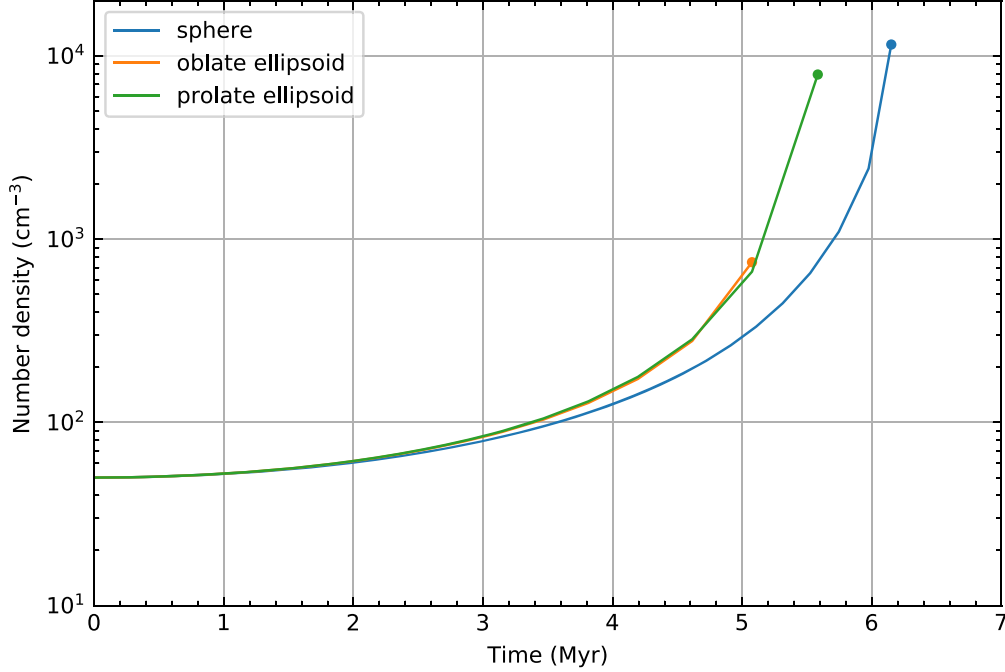


Figure 1. The number density as a function of time in different collapsing models (sphere, oblate ellipsoid, and prolate ellipsoid). Note that their end time points are determined by the morphology, initial density, and final semiminor axis.

the prolate and oblate ellipsoids are mainly concentrated on their short axis, which leads to a more rapid change in volume and density for the prolate one. Their final number densities are slightly artificial due to the range of typical scales, but it does not change the conclusion that the prolate one has a higher final number density. The oblate spheroid approaches a thin disk at final time, while the prolate spheroid becomes a thin cylinder. In general, the dynamics for collapsing clouds with different shapes have a great difference at late stages.

3.3. The Static Spherical Cloud

The solution of self-similar collapse of isothermal spheres shows that an r^{-2} law holds for the density distribution in the static or nearly static outer envelope (e.g., Bodenheimer & Sweigart 1968; Shu 1977). Since the central density is infinite with this density distribution, we adopt another treatment as Lee et al. (1996), where the total hydrogen number density $n_{\text{H}} = n(\text{H}) + 2n(\text{H}_2)$ as a function of radius varies as

$$n_{\text{H}} = \frac{n_{\text{H,max}}}{\left(1 + \frac{c \cdot r}{r_{\text{max}}}\right)^2}, \quad (11)$$

where $n_{\text{H,max}}$ is the hydrogen density at the cloud center ($r=0$), r_{max} is the cloud radius, and c is a constant. If the number density at the cloud surface $n_{\text{H,min}}$ is known, we can get the

value of the constant c as

$$c = \left(\frac{n_{\text{H,max}}}{n_{\text{H,min}}}\right)^{1/2} - 1. \quad (12)$$

3.4. Physical Parameters

We assume that these clouds are exposed to the Draine (1978) interstellar radiation field (equal to ~ 1.7 times the Habing (1968) local interstellar field), which may be multiplied by an intensity scaling factor G_0 to represent a different radiation. The interstellar medium near an early-type star is exposed to strong UV radiation field, so we investigate the influence of strong radiation field on H, H₂, CO and OH abundances in Section 5.3. The cosmic-ray ionization rate is adopted as $3 \times 10^{-17} \text{ s}^{-1}$ for the majority of this paper (Clark et al. 2019). Observations for some objects under different interstellar environments, using tracers such as H₃⁺, indicate that there is a wide range of cosmic-ray ionization rate, from a few times 10^{-18} to a few times 10^{-14} s^{-1} (e.g., Hartquist et al. 1978; van der Tak & van Dishoeck 2000; Shaw et al. 2008; Indriolo et al. 2010, 2015; Indriolo & McCall 2012). Thus we also study the influence of different cosmic-ray ionization rates on H, H₂, CO and OH abundances in Section 5.4. We assume dust is characterized by a representative grain radius $a = 0.1 \mu\text{m}$ and an average albedo of 0.6. The material density of dust is taken to be 2 g cm^{-2} and the dust-to-gas mass ratio is

Table 2
Initial Abundances with Respect to Total Hydrogen

First Type (H)		Second Type (H/H ₂)		Third Type (H ₂)	
Species	Abundance	Species	Abundance	Species	Abundance
H	$-2 \times 10^{-5} + 1$	H	variable	H	0.0
H ₂	1×10^{-5}	H ₂	variable	H ₂	5×10^{-1}
He	9×10^{-2}	He	9×10^{-2}	He	9×10^{-2}
C ⁺	1.4×10^{-4}	C ⁺	1.4×10^{-4}	C ⁺	1.4×10^{-4}
N	7.5×10^{-5}	N	7.5×10^{-5}	N	7.5×10^{-5}
O	3.2×10^{-4}	O	3.2×10^{-4}	O	3.2×10^{-4}
S ⁺	8×10^{-8}	S ⁺	8×10^{-8}	S ⁺	8×10^{-8}
Si ⁺	8×10^{-9}	Si ⁺	8×10^{-9}	Si ⁺	8×10^{-9}
Fe ⁺	3×10^{-9}	Fe ⁺	3×10^{-9}	Fe ⁺	3×10^{-9}
Mg ⁺	7×10^{-9}	Mg ⁺	7×10^{-9}	Mg ⁺	7×10^{-9}
Cl ⁺	4×10^{-9}	Cl ⁺	4×10^{-9}	Cl ⁺	4×10^{-9}
Na ⁺	2×10^{-9}	Na ⁺	2×10^{-9}	Na ⁺	2×10^{-9}
P ⁺	3×10^{-9}	P ⁺	3×10^{-9}	P ⁺	3×10^{-9}
F	4×10^{-9}	F	4×10^{-9}	F	4×10^{-9}

Note. H, H/H₂, and H₂ represent respectively the model in which hydrogen is mainly atomic, shell-dependent H/H₂ ratio, molecular initially in all shells.

taken to be 0.01. The surface site density is taken to be 1×10^{15} cm⁻², and the chemical desorption efficiency is taken to be 0.05 (Du 2021). The main energy coupling of gas and dust is through gas-grain collisions. Bergin & Tafalla (2007) reviewed that the gas and dust tend to couple thermally via frequent collisions at high densities ($>10^4$ cm⁻³), and their temperatures are expected to converge. Furthermore, the gas and dust in low density regions are thermally decoupled due to inadequate collisions, and the gas becomes warmer than the dust due to photoelectric heating. In a few hundred number density photodissociation region, both observations and theoretical calculations indicate the gas temperature is about 30 K (Wolfire et al. 2003; Tielens 2010), and that dust temperature is close to a value of 15 K (Ward-Thompson et al. 2002; Bianchi et al. 2003; Tielens 2010), so we adopt these values in this work. We also study the influence of different gas and dust temperature on H, H₂, CO, and OH abundances in Section 5. These physical parameters are summarized in Table 1.

Since these clouds that we study are spherical, a weighting factor for each shell should be applied to calculate the column density for species *X*, which boosts the importance of outer shells and lower the importance of inner shells. We define a weighted column density $N(X)$ for species *X* as (Lee et al. 1996)

$$N(X) = A \sum_i \left[n_i(X) dL_i \left(\frac{r_i}{r_{\max}} \right)^2 \right], \quad (13)$$

where A is a normalization constant, $n_i(X)$ is the number density for species *X* in shell *i*, dL_i is the width of shell *i*, r_i is the distance from the center for shell *i*, and r_{\max} is the cloud radius. The relation between the visual extinction A_V and the total column density of protons N_H is $A_V = 5.34 \times 10^{-22} N_H$

(Bohlin et al. 1978). To study the influence of different clouds and initial abundances, we define the weighted column density for species *X* relative to total column density as the average abundance $f(X) = N(X)/(2N(H_2) + N(H))$.

3.5. Initial Abundances

To figure out the effect of the initial chemical compositions on the chemical evolution, we select three types of initial chemical compositions listed in Table 2 (McElroy et al. 2013; Du 2021). In the first type, we assume that hydrogen is completely atomic initially for all shells. In the second type, the initial abundances except H and H₂ are the same as in the first type. For the initial abundances of H and H₂, we run our code with the first type initial conditions in all shells for a certain amount of time, and use the final abundances of H and H₂ as their initial abundances. For these static clouds, we adopt the H/H₂ abundances at a time of 1×10^6 yr as their initial abundances in the second type. For these collapsing spherical or ellipsoidal clouds, we adopt the H/H₂ abundances at $t = 6.15 \times 10^6$ yr (equal to collapsing timescale of a uniform spherical cloud) as their initial abundances. In the third type, we start with molecular hydrogen in all shells. Based on cloud types and initial chemical compositions, in total, 12 models listed in Table 3 are constructed, which are labeled Model 1–12.

4. Results

The H atoms in gas phase are reduced by adsorbing on the dust grain surfaces. The formation of H₂ molecules on dust grain surfaces is treated as a normal two-body surface reaction: $gH + gH \rightarrow gH_2$ in our models, which is different from some

Table 3
Cloud Types and Initial H/H₂ Abundances in Different Models

Model	Initial hydrogen		
Cloud	H	H/H ₂	H ₂
Gravitationally collapsing uniform spherical cloud	Model 1	Model 2	Model 3
Gravitationally collapsing uniform oblate ellipsoidal cloud	Model 4	Model 5	Model 6
Gravitationally collapsing uniform prolate ellipsoidal cloud	Model 7	Model 8	Model 9
Static spherical cloud	Model 10	Model 11	Model 12

of previous works (as Li & Goldsmith 2003; Holdship et al. 2017). The CO molecules are mainly produced in gas phase, and removed from the gas through photodissociation, cosmic-ray-induced photodissociation and adsorption reactions. The OH molecules for different time are dominated by different reactions. Studying their abundances is helpful in constraining the initial compositions and evolution history of clouds.

4.1. The Gravitationally Collapsing Uniform Spherical Cloud

Initially the cloud has a radius of 16.8 pc and total mass of $3.4 \times 10^4 M_{\odot}$, which are selected so that the mass and spatial and dynamical scale mimic those of observed molecular clouds. The initial number density of the cloud is 50 cm^{-3} , and the cloud collapse timescale is $6.2 \times 10^6 \text{ yr}$. The cloud radius changes from 16.8 to 2.7 pc, when the number density changes from 50 to $1.2 \times 10^4 \text{ cm}^{-3}$. The total column density increases by a factor of about 2 for the spherical cloud.

Figure 2 shows the abundance profiles for H, H₂, CO, and OH at different time in models 1–3. Since the results in Model 1 and 2 are similar, we discuss them in Model 1 as an example. The cloud radius begins to change appreciably at $t \sim 4 \times 10^6 \text{ yr}$, leading to the increasing number density and boosted reaction rates in models 1–3. In Model 1, the H₂ abundance for $t \sim 6 \times 10^6 \text{ yr}$ is characterized by an essentially flat profile, with abundance ~ 0.5 , when the H abundance for all radius is low, being more abundant outwards. At the same time, the abundance of CO and OH for inner radius respectively reaches 4×10^{-5} and 4×10^{-7} , while their abundances in outer layers are still extremely low due to intensive UV photons. In Model 3, the OH abundance for inner radius is lower than in Model 1 at late time. This is mainly because H atoms can accelerate OH formation by two major reactions: $\text{O} + \text{H} \rightarrow \text{OH}$ in gas phase and on dust grain surfaces. In the absence of H atoms, OH molecules are slowly produced by the reaction: $\text{O} + \text{H}_2\text{S}^+ \rightarrow \text{HS}^+ + \text{OH}$. The central HI density at late time is close to 1 cm^{-3} , which is in reasonable agreement with the value in Li & Goldsmith (2003). The H atoms on dust grain surfaces can effectively form H₂ molecules before desorption, so the H₂ formation efficiency is close to unity (Li &

Goldsmith 2003). Note that the central HI density at a high dust temperature is clearly higher than 1 cm^{-3} due to low H₂ formation efficiency, and we discuss in detail the reason in Section 5.2.

Figure 3 shows the average abundances for above four species varying with time in models 1–3. For models 1–3, the collapsing clouds at early time are the pre-CO phases, when CO has not formed in sufficient quantity to be detectable, and OH molecules are also difficult to detect. The average abundance of CO and OH in models 1–2 respectively grows to 5×10^{-5} and 3×10^{-7} , which is close to their typical values in molecular clouds, when the cloud radius shrinks to $\sim 3 \text{ pc}$. At this time, the HI column density is close to 10^{20} cm^{-2} , which is identical with its observed value in Wannier et al. (1983). Accordingly, the collapsing spherical clouds in which hydrogen is mainly atomic initially can match the observational characteristics of molecular clouds. The OH abundance in Model 3 is lower than its minimum value of 5.7×10^{-8} in molecular clouds from Tang et al. (2021), which suggests the collapsing cloud in which hydrogen is molecular initially cannot match OH abundance in typical molecular clouds.

4.2. The Gravitationally Collapsing Uniform Ellipsoidal Cloud

Oblate or prolate ellipsoidal clouds are axisymmetric, so we only discuss the abundance distributions for H, H₂, CO and OH in two-dimensional space. The oblate ellipsoidal cloud has an initial number density of 50 cm^{-3} and total mass of $1.4 \times 10^4 M_{\odot}$. The semimajor axis is 16.8 pc and semiminor axis is 6.7 pc. The cloud collapse timescale is $5.4 \times 10^6 \text{ yr}$. Here we mainly show the variation of physical parameters along the short axis, which are mainly determined by the shortest distance from cloud surface. At the final stage of our modeling, the semiminor axis shrinks to 0.9 pc, and the number density is about 750 cm^{-3} . The column density increases by a factor of about 2 for the oblate ellipsoidal cloud. We also model a prolate ellipsoidal cloud, using another set of physical parameters. These physical parameters for oblate and prolate ellipsoidal clouds are listed in Table 4.

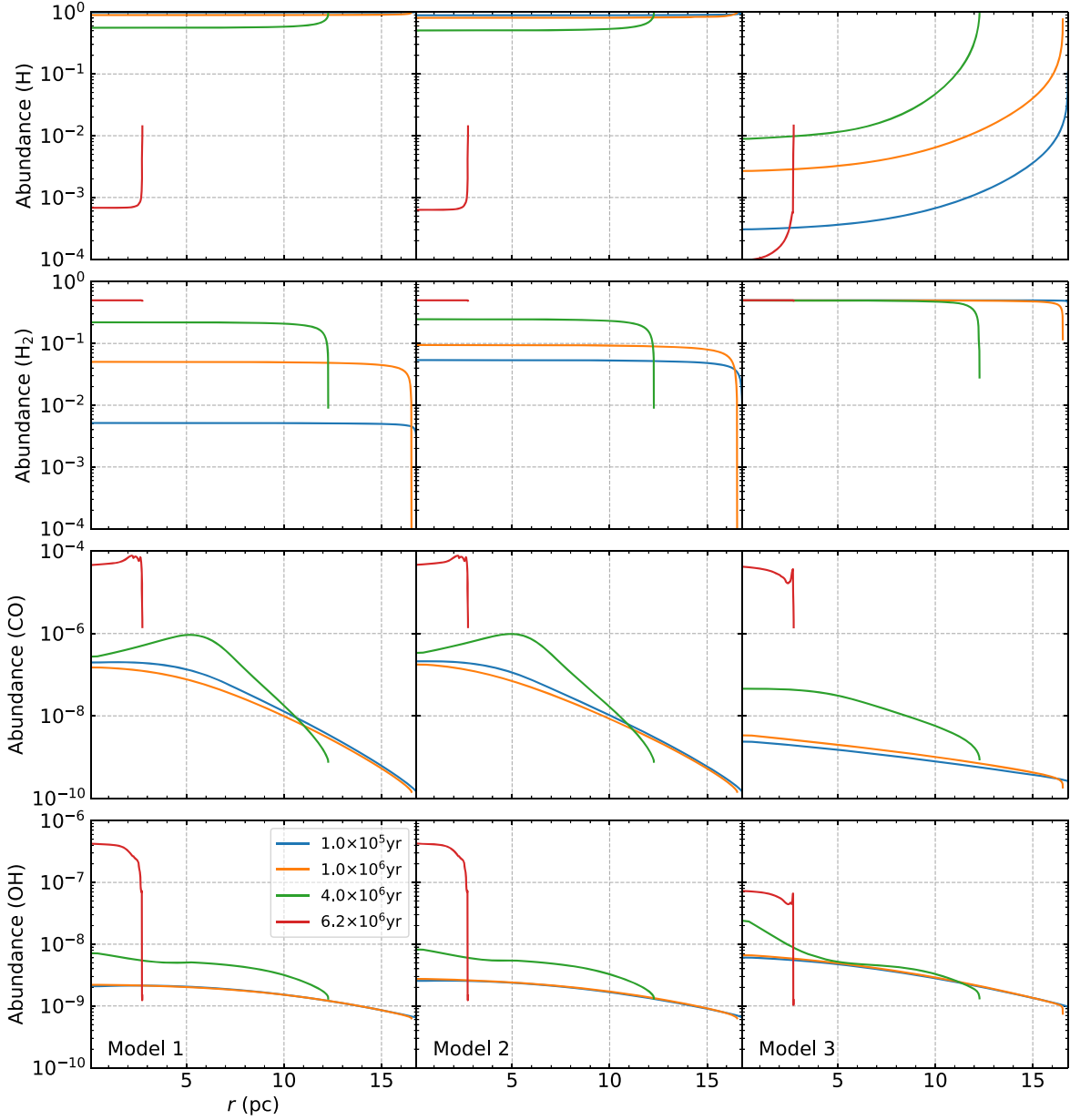


Figure 2. The abundances of H, H₂, CO, and OH as a function of radius r in a gravitationally collapsing uniform spherical cloud at various time using models 1–3. Note that as time goes on, the cloud shrinks, and the ends of the curves move toward inner radius.

To save space, we put the abundance maps for H, H₂, CO and OH in the [Appendix](#). Figures A1–A8 show their abundance distributions at different time in models 4–9. The H₂ abundance in models 7–8 is more abundant than in models 4–5 at late times, suggesting the transition from H to H₂ is fast in high density $>750 \text{ cm}^{-3}$ regions. For $t = 5.4 \times 10^6 \text{ yr}$, H₂ molecules in Model 7 have been produced in large quantity, so the cloud is mainly composed of molecular hydrogen. At the final stage, CO and OH molecules for models 4–5 are not formed in large quantity, while for models 7–8 their abundances reach a high

level due to high number density. The behaviors for these four species in Model 6 are different from in Model 9. At late time, the abundances for H₂, CO and OH in Model 9 are more abundant than in Model 6, suggesting higher chemical reaction rates in Model 9. In general, there are some differences in abundances of some species (e.g., OH, CO) between the oblate and prolate ellipsoid, which are mainly due to their different evolution of number density (see Section 3.2). Namely, differences in clouds shape can lead to their differences in chemical evolution via the number density.

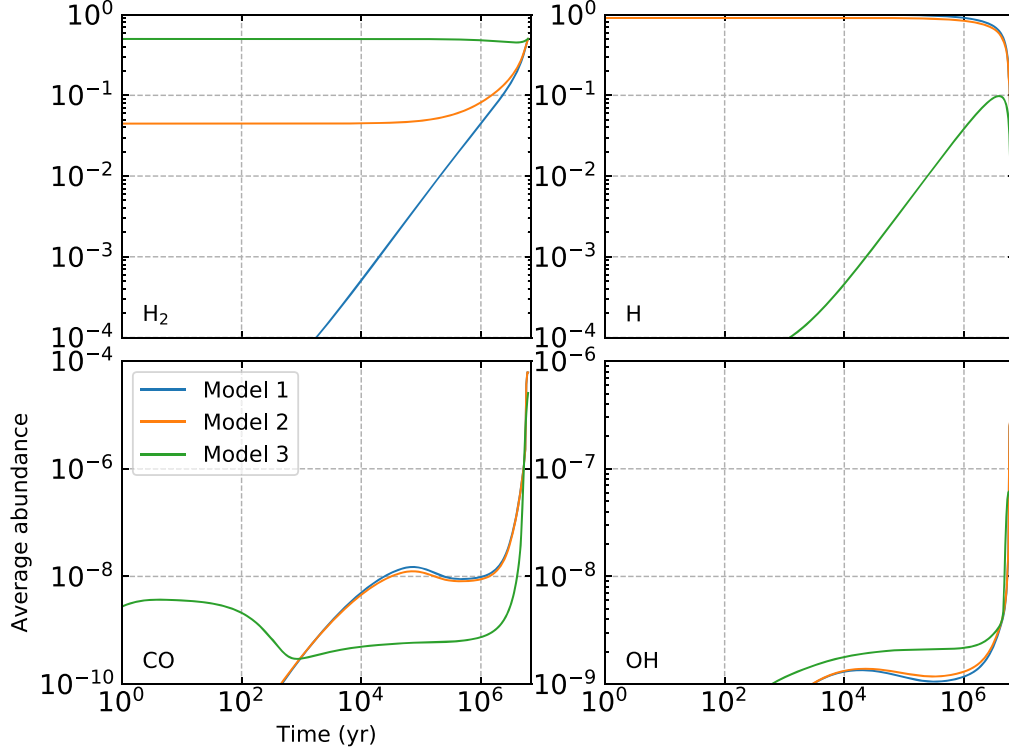


Figure 3. The average abundances for H, H₂, CO, and OH as a function of time using models 1–3.

Table 4
Physical Parameters for Oblate and Prolate Ellipsoidal Clouds

	Oblate Ellipsoidal Cloud	Prolate Ellipsoidal Cloud
Initial number density (cm ⁻³)	50	50
Mass (M_{\odot})	1.4×10^4	6.9×10^4
Initial semimajor (pc)	16.8	33.6
Initial semiminor axis (pc)	6.7	16.8
Collapse timescale (yr)	5.4×10^6	5.8×10^6
Final semiminor axis (pc)	0.9	1.6
Final number density (cm ⁻³)	750	7928

4.3. The Static Spherical Cloud

The number density of the cloud as a function of radius is described in Section 3.3. Here, we take the number density at the cloud center $n_{\text{H,max}} = 1 \times 10^4 \text{ cm}^{-3}$ and the number density at the cloud surface $n_{\text{H,min}} = 1 \times 10^2 \text{ cm}^{-3}$. The static cloud has a total radius of 7 pc, total visual extinction A_V of 10.4 mag, and total mass of $1.1 \times 10^4 M_{\odot}$. Some observations for Class I clouds have shown their lifetime is limited to a few Myr, which represent the duration of the “inert” CO phase without massive star formation (e.g., Fukui et al. 1999;

Kawamura et al. 2009). Hence the chemical modeling time is taken to be $8 \times 10^6 \text{ yr}$ in these static models.

Figure 4 shows the abundance profiles for H, H₂, CO, and OH at different time in models 10–12. The CO abundance for inner radius begins to decrease due to adsorption at $t \sim 10^6 \text{ yr}$ in these static models, which is different from some works leaving CO adsorption out of account (e.g., Lee et al. 1996). At late time, the OH abundance of $\sim 10^{-6}$ for inner radius in Model 10 is clearly higher than its value of $\sim 10^{-7}$ in Model 12, which resembles the collapsing models. There is a noteworthy rapid change for H, CO, and OH abundances at $r \sim 2.3 \text{ pc}$ in these static models, corresponding to a visual extinction of $\sim 2.0 \text{ mag}$. Our preliminary investigation suggests that the rapid change may be related to bistable solutions (low-ionization phase and high-ionization phase) in the nonlinear kinetic equations (e.g., Pineau des Forets et al. 1992; Le Boulrot et al. 1993), and we plan to clarify this phenomenon in a future work due to its complexity.

Figure 5 shows the average abundances for above four species varying with time in models 10–12. For models 10–11, the CO and OH average abundances at $t \sim 10^6 \text{ yr}$ reach a high level, when the HI column density of $\sim 8 \times 10^{21} \text{ cm}^{-2}$ cannot match what has been observed (e.g., Wannier et al. 1983; Bigiel et al. 2008; Lee et al. 2012). The CO abundance for late time reaches a low level of 4×10^{-6} due to CO freeze out,

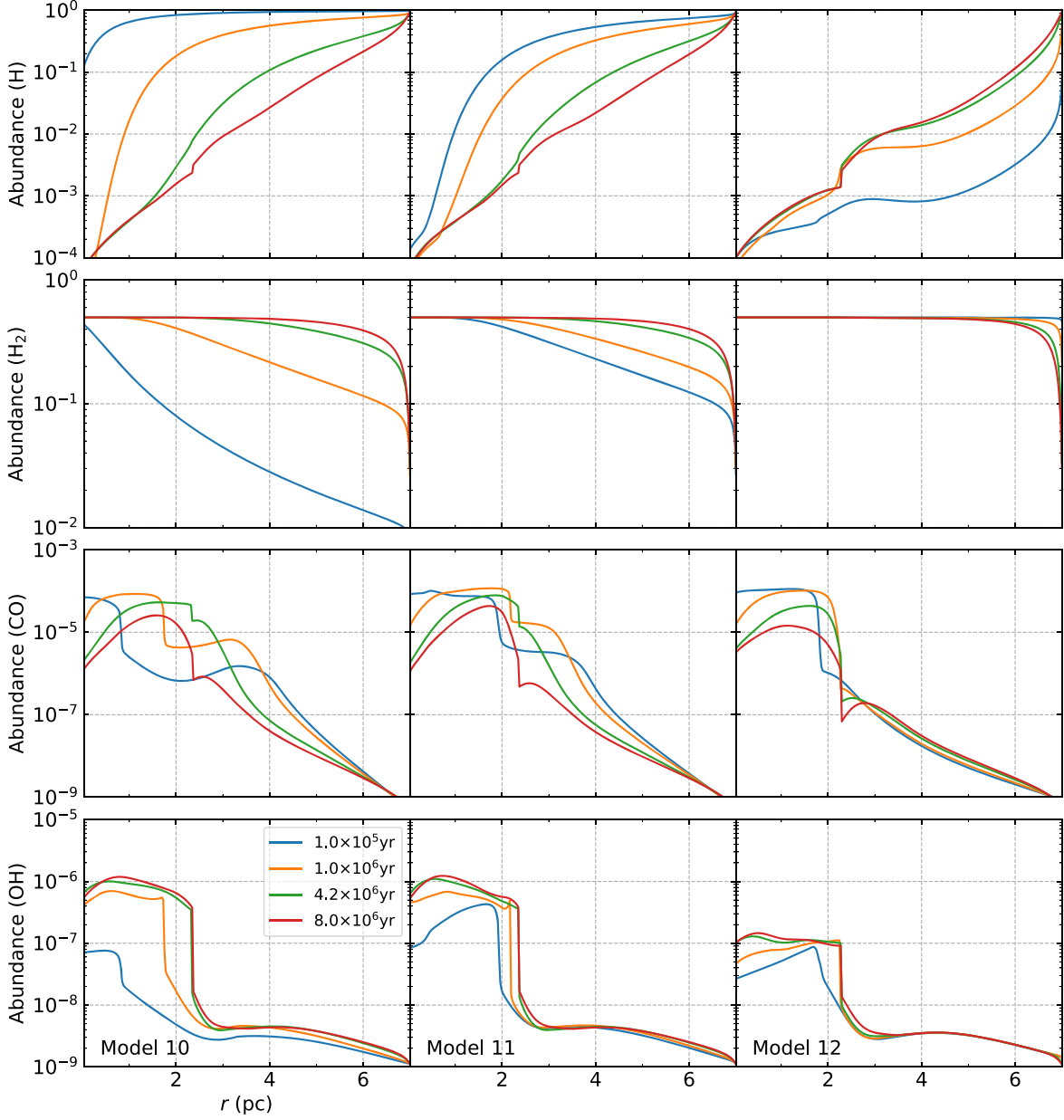


Figure 4. The abundances of H, H₂, CO and OH as a function of radius r in a static spherical cloud at various time using models 10–12.

when the OH abundance of $\sim 2 \times 10^{-7}$ is growing, so the CO-poor cloud may be traced by OH. It reveals that a molecular cloud with typical physical parameters cannot stay static for a long time and still be observable in CO. Accordingly, these static clouds in which hydrogen are mainly atomic initially cannot match observational characteristics, unless we adopt the argument from Seifried et al. (2022) that the underestimation of HI column density is due to both the large HI temperature

variations and the effect of noise in regions of high optical depth, and real HI column densities of $\gtrsim 10^{22} \text{ cm}^{-2}$ are frequently reached in molecular clouds. In Model 12, the HI average abundance for $t > 10^6$ yr can match their observed values in molecular clouds, while the OH abundance for all time is lower than its observed value of 5×10^{-8} (Crutcher 1979). Hence the static cloud in which hydrogen is molecular initially also cannot match OH observed abundance

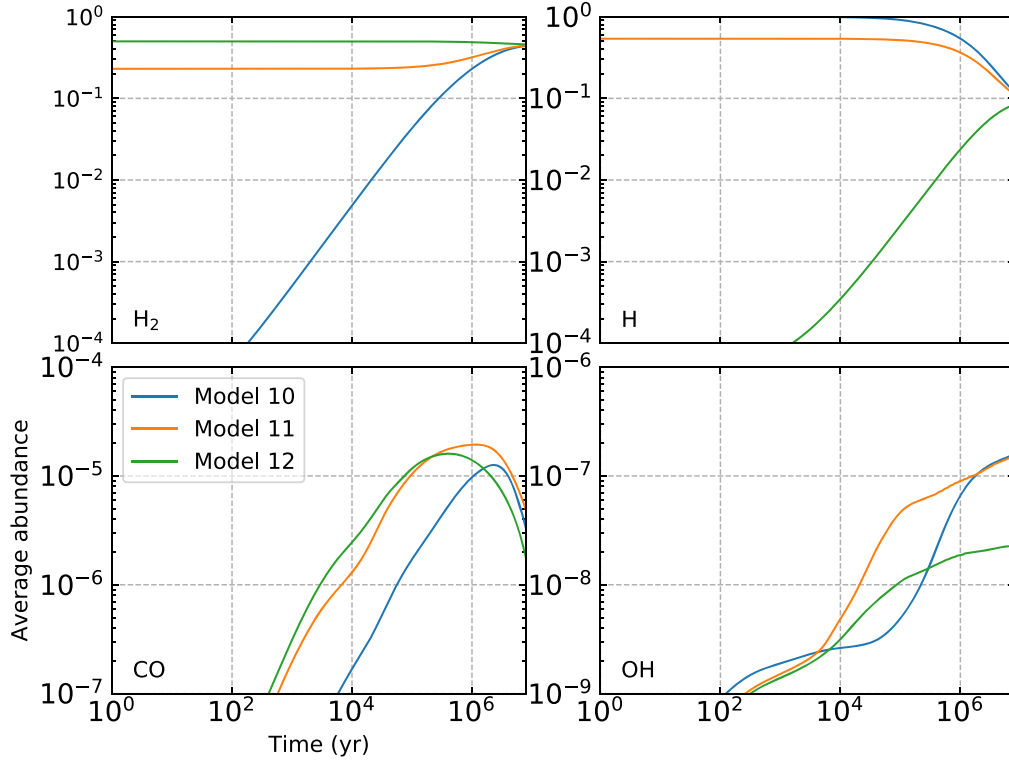


Figure 5. The average abundances for H, H₂, CO, and OH as a function of time using models 10–12.

in typical molecular clouds. In short, the static clouds cannot match observational characteristics in typical molecular clouds, which is one main reason why we consider collapsing models.

5. The Influence of Some Physical Parameters on Chemical Evolution

In previous sections we have assumed constant value for some physical parameters (T_{gas} , T_{dust} , G_0 , and ζ). Here we study whether adopting other values for them might affect chemical evolution, using the static models as an example. To obtain appropriate values of physical parameters, we analyze the influences of above four physical parameters on H₂, being the most important molecule in clouds.

5.1. Insensitivity to Gas Temperature

The relationship between the H adsorption rate coefficient k_{H} and gas temperature is given by $k_{\text{H}} \propto T_{\text{gas}}^{1/2}$ (Du 2021), so H₂ formation is accelerated with increasing gas temperature. We select a high gas temperature of 100 K to study the changes in H, H₂, CO, and OH average abundances. We find the average abundances of H, CO, and OH do not change appreciably, relative to the case with $T_{\text{gas}} = 30$ K. Namely, chemical evolution is insensitive to gas temperature when it is lower than 100 K.

5.2. Dependence on Dust Temperature

The competition between desorption and diffusion rate of H atoms on dust grain surfaces leads to great differences in H₂ formation efficiency at different dust temperature. The H thermal desorption rate dominating its evaporation is given by

$$k_{\text{des}} = 2.74 \times 10^{12} \text{ s}^{-1} \exp(-450 \text{ K}/T_{\text{dust}}), \quad (14)$$

and the diffusion rate for H atoms k_{diff} is

$$k_{\text{diff}} = 2.1 \times 10^6 \text{ s}^{-1} \exp(-225 \text{ K}/T_{\text{dust}}), \quad (15)$$

obtained using the H desorption energy of 450 K, a rectangular barrier with a height of 225 K, and the number of sites on a grain surface of 1.3×10^6 (Du 2021). When the H desorption rate equals its diffusion rate, the dust temperature is close to ~ 16 K. The H atoms can scan all of the adsorption sites before desorption at dust temperature below ~ 16 K, so the H₂ formation rate is determined by the H adsorption rate (independent of dust temperature). When the dust temperature is higher than ~ 16 K, considerable H atoms go back to the gas phase before meeting their reaction partners, resulting the H₂ formation efficiency is significantly lower than unity. Hence we select a high dust temperature of 20 K to study how it affects chemical evolution in Figure 6.

At $T_{\text{dust}} = 20$ K, the static clouds at late time using models 10–12 is far from reaching chemical equilibrium. This is

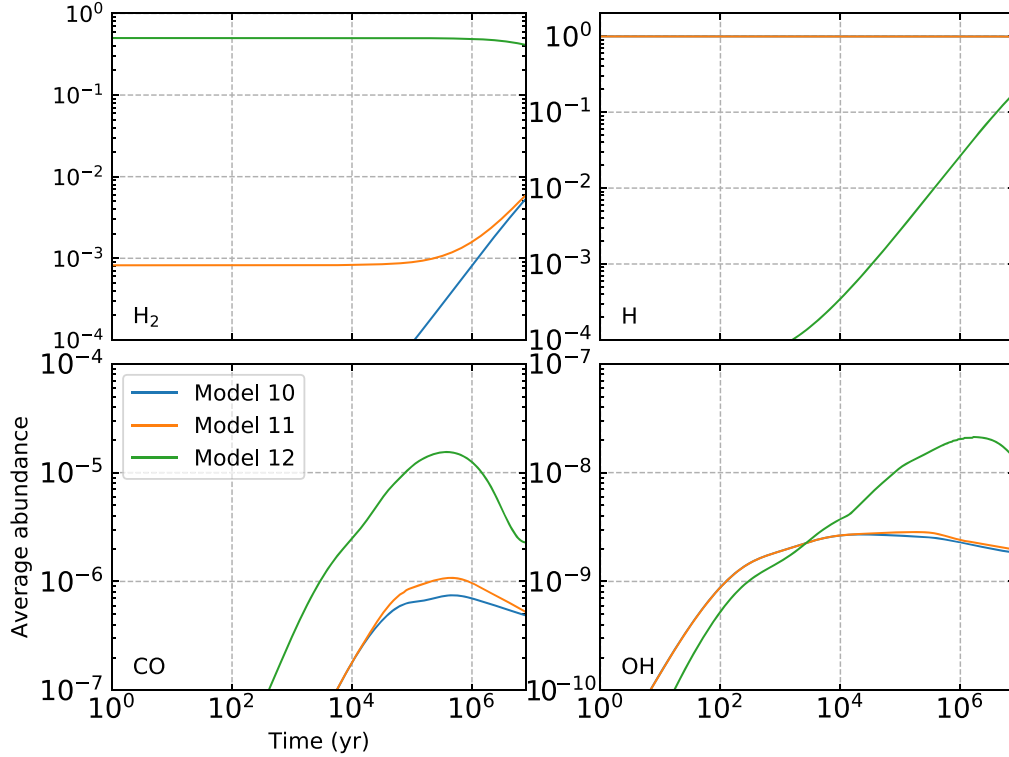


Figure 6. The average abundances for H, H₂, CO, and OH as a function of time using models 10–12 with $T_{\text{dust}} = 20$ K.

mainly because the desorption rates for some species on dust grain surfaces are boosted with increasing dust temperature, resulting in some surface reactions become inefficient. In Model 10–11, the abundances of H₂, CO and OH are different from in Figure 5, which suggests some important molecules formed on dust grain surfaces heavily depend on the dust temperature. In Model 12, the average abundances for these four species at $T_{\text{dust}} = 20$ K seem to not change appreciably relative to Figure 5 with $T_{\text{dust}} = 15$ K. Therefore, CO clouds are difficult to form at high dust temperatures, which is one reason why most observed dust temperatures in molecular clouds are lower than 20 K (e.g., Bianchi et al. 2003; Kramer et al. 2003; Schnee & Goodman 2005). In general, the static clouds with a high dust temperature cannot match observational characteristics.

5.3. Variation with the Intensity of Interstellar Radiation Field

The H₂ photodissociation rate is closely correlated with the H₂ self-shielding and shielding by dust (Draine & Bertoldi 1996), so the effect of interstellar radiation field (ISRF) on H₂ is mainly limited to the outer layers of clouds. The intensity of radiation field (G_0) near a star can easily exceed 1000. Therefore, we adopt models 10–12 with $G_0 = 1000$ in Figure 7 to study chemical evolution.

In models 10–12 with a strong ISRF, the abundances of H₂, CO and OH for all time are much lower relative to Figure 5 with a weak ISRF. At $t \sim 10^6$ yr, the CO abundances in these models are close to 4×10^{-6} , so these static clouds are CO-poor. The CO molecules in molecular clouds exposed to strong ISRF can only exist in large quantities for a short time, which is one reason why molecular clouds near early-type stars become quickly undetectable in CO (e.g., Hartmann et al. 2001). At this time, these static clouds are mainly atomic, and their HI column density of $\sim 10^{22}$ cm⁻² exceed observed upper threshold of a few 10^{21} cm⁻². In general, the static clouds with a strong ISRF cannot match observational characteristics in typical molecular clouds.

5.4. Variation with Cosmic-Ray Ionization Rate

The observed cosmic-ray ionization rates as traced by H₃⁺ are mostly in a narrow range in the Galactic diffuse interstellar medium and molecular clouds, from a few times 10^{-17} s⁻¹ to a few times 10^{-16} s⁻¹ (e.g., McCall et al. 1999; Indriolo & McCall 2012). The cosmic-ray ionization rates near Supernova Remnant IC 443 and toward the Galactic center are in a range, from a few times 10^{-16} s⁻¹ to a few times 10^{-14} s⁻¹ (e.g., Hartquist et al. 1978; Geballe & Oka 2010; Indriolo et al. 2010). Accordingly, the cosmic-ray ionization rates in different interstellar medium have a great difference. The attenuation of

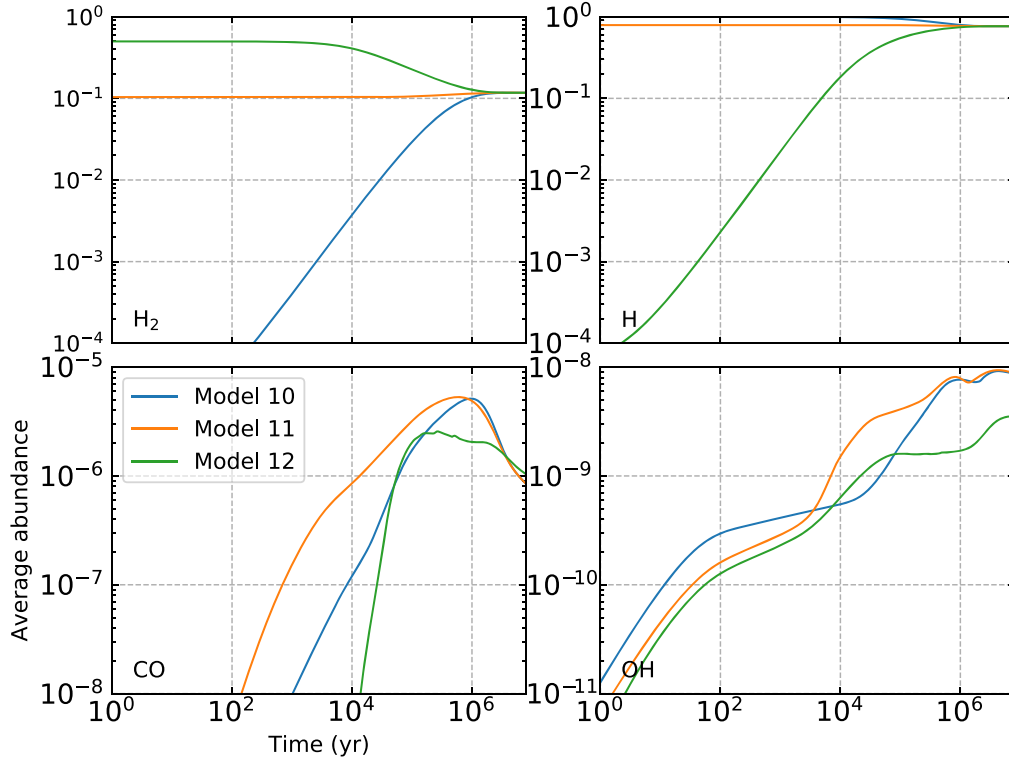


Figure 7. The average abundances for H, H₂, CO, and OH as a function of time using models 10–12 with $G_0 = 1000$. The intensity scaling factor G_0 is defined by the actual radiation field relative to Draine (1978) radiation field.

cosmic rays is negligible (Umebayashi & Nakano 1981) at column density below $4 \times 10^{25} \text{ cm}^{-2}$, so intensive cosmic rays greatly influence the molecules formation for all positions. Thus we adopt a high cosmic-ray ionization rate (ζ) of $3 \times 10^{-15} \text{ s}^{-1}$ to study chemical evolution, and the results are shown in Figure 8.

When the cosmic-ray ionization rate is adopted as $3 \times 10^{-15} \text{ s}^{-1}$, these static clouds at late time are mainly composed of molecular hydrogen, but the CO and OH abundances are extremely low. The observation for CO-dark molecular gas indicates that OH column density ranges from 10^{12} to 10^{14} cm^{-2} , that the upper limit of CO column density is $5 \times 10^{14} \text{ cm}^{-2}$ at a CO sensitivity of 0.25 K, and that HI column density is from 10^{20} to 10^{21} cm^{-2} (Li et al. 2018). Hence these static clouds for late time where CO column density is close to $\sim 4 \times 10^{14} \text{ cm}^{-2}$ may be CO-dark, whereas they have a high OH column density of $\sim 10^{14} \text{ cm}^{-2}$ and may be detectable with OH absorption. In Model 12, the abundances of CO and OH basically reach their respective maximum of 10^{-6} and 6×10^{-8} at $t \sim 10^4 \text{ yr}$, then the static cloud mainly composed of molecular hydrogen quickly becomes transparent in CO and OH. Accordingly, CO and OH molecules in clouds with intensive cosmic rays cannot exist in large quantities for a long time, unless in some high density regions. In general, the static

clouds with intensive cosmic rays cannot match observational characteristics in typical molecular clouds.

6. Discussions

The treatments of initial abundances are simple in many chemical simulations (e.g., Hasegawa et al. 1992; Garrod & Pauly 2011), but initial chemical compositions can greatly affect the chemical evolution. Therefore, we study three types of initial abundances for each type of clouds (collapsing clouds, and static clouds) in Section 4. The chemical evolution in these clouds shows that the models in which hydrogen is mainly atomic initially (e.g., Model 1) seem excel the models in which hydrogen is mainly molecular initially (e.g., Model 3) in matching the observational characteristics in molecular clouds. Accordingly, we suggest that initial chemical compositions of molecular clouds are mainly atomic hydrogen. This means CO molecules are able to form even without the pre-existence of H₂.

The dynamics of clouds is an important factor affecting the chemical evolution of clouds. Thus we show the chemical evolution (e.g., H, H₂, CO and OH) in three types of clouds with different dynamics in Section 4. Chemical evolution in these clouds with identical initial chemical compositions (e.g., models 1 and 10) shows that the collapsing models are better

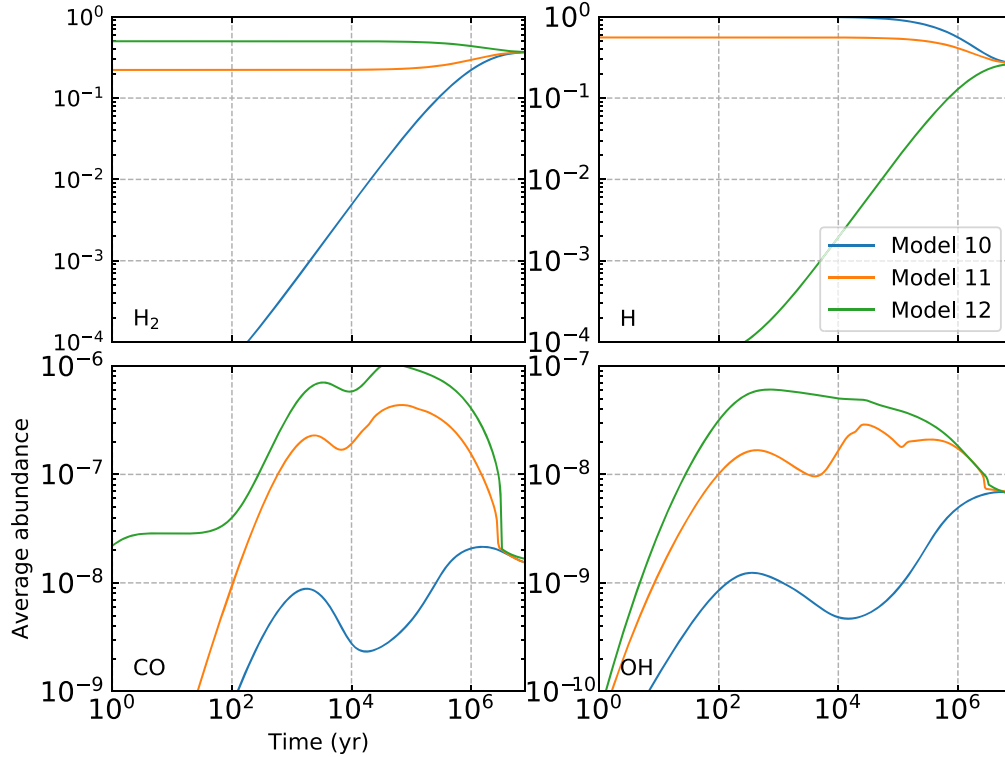


Figure 8. The average abundances for H, H_2 , CO, and OH as a function of time using models 10–12 with a cosmic-ray ionization rate of $3 \times 10^{-15} \text{ s}^{-1}$.

than the static models in matching the observational characteristics in molecular clouds. This is mainly because gravity can enhance the reaction rates by increasing the number density during collapse, then speeds up the formation of some important molecules (e.g., H_2 , CO, OH). The differences in morphology between prolate, oblate, and spherical clouds lead to large differences in chemical evolution, via some differences in the evolution of number density (see Section 3.2).

In Section 5, we explore whether adopting other values for some important physical parameters might affect the conclusions in static models. Some important molecules heavily depend on the dust temperature, so the heating and cooling mechanisms should be taken into consideration, to automatically solve the temperature in tandem with chemical abundances (e.g., as done in Du & Bergin 2014). Under the circumstances of high dust temperature, strong radiation field, and intensive cosmic rays; the static models seem unable to match the observational characteristics in molecular clouds. Namely, some important molecules (e.g., H_2 , CO) in clouds are easier to form under typical molecular clouds environment.

The uncertainties in the magnetic fields strength and the turbulence, together with a possible revision of the lifetimes of the molecular gas (e.g., Hartmann et al. 2001), have resulted in two opposed views of clouds lifetime, including a long cloud

lifetime of at least 10 Myr (e.g., Mouschovias et al. 2006; Schinnerer et al. 2013) and a short cloud lifetime of 3–5 Myr (e.g., Hartmann 2003; Vázquez-Semadeni et al. 2003). From a chemical modeling perspective, the CO cloud lifetime estimates do not include any earlier phase when the gas is dominantly molecular but CO has not formed in sufficient quantity for detectable emission (Bergin & Tafalla 2007). In our models in which hydrogen is mainly atomic initially, the above earlier phases do not seem to exist, so CO cloud lifetime estimates are not affected. At high gas temperature, strong radiation field, and intensive cosmic rays regions as in Section 5; CO clouds in such environments are transient due to rapid CO destruction (related to CO adsorption, photodissociation, and cosmic-ray-induced photodissociation reactions).

7. Conclusions

In this paper, we model chemical evolution for collapsing spherical, collapsing ellipsoidal clouds, and static clouds using three types of initial abundances. We also study the influence of gas temperature, dust temperature, intensity of interstellar radiation field, and cosmic-ray ionization rate on chemical evolution in static clouds. Our conclusions are as follows:

1. The collapsing models are better than the static models in matching the observational characteristics in typical

molecular clouds. This is mainly because gravity can speed up the formation of some important molecules (e.g., H_2 , CO , OH) by increasing the number density during clouds collapse.

2. The differences in morphology between prolate, oblate, and spherical clouds can lead to differences in chemical evolution, which are mainly due to their different evolution of number density.
3. In the framework of our modeling, H atoms can accelerate OH formation by two major reactions: $\text{O} + \text{H} \rightarrow \text{OH}$ in gas phase and on dust grain surfaces, as a consequence the models in which hydrogen is mainly atomic initially perform better than the models in which hydrogen is mainly molecular initially in matching observations. Therefore, we suggest the initial

chemical compositions of molecular clouds to be mainly atomic hydrogen.

4. Under the circumstances of high gas temperature, strong radiation field, and intensive cosmic rays, the static CO clouds are transient due to rapid CO destruction.

Acknowledgments

This work is financially supported by the National Natural Science Foundation of China through grants 12041305 and 11873094.

Appendix Figures in Collapsing Ellipsoidal Clouds

In this section, we show the abundance distribution for H, H_2 , CO and OH at different time in two-dimensional space in collapsing ellipsoidal clouds (Figures A1–A8).

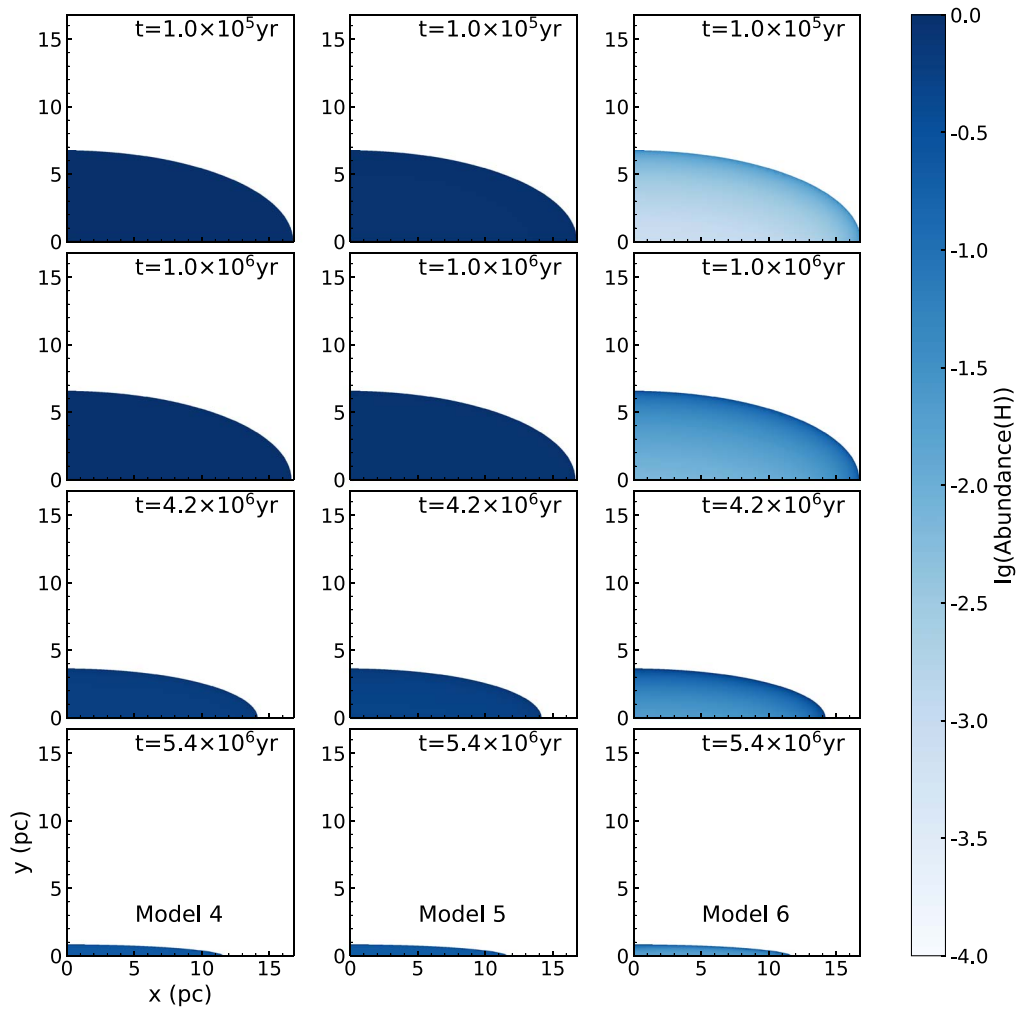


Figure A1. The H abundance distribution at different time in a gravitationally collapsing uniform oblate ellipsoidal cloud using models 4–6. Note that as time goes on, the cloud shrinks.

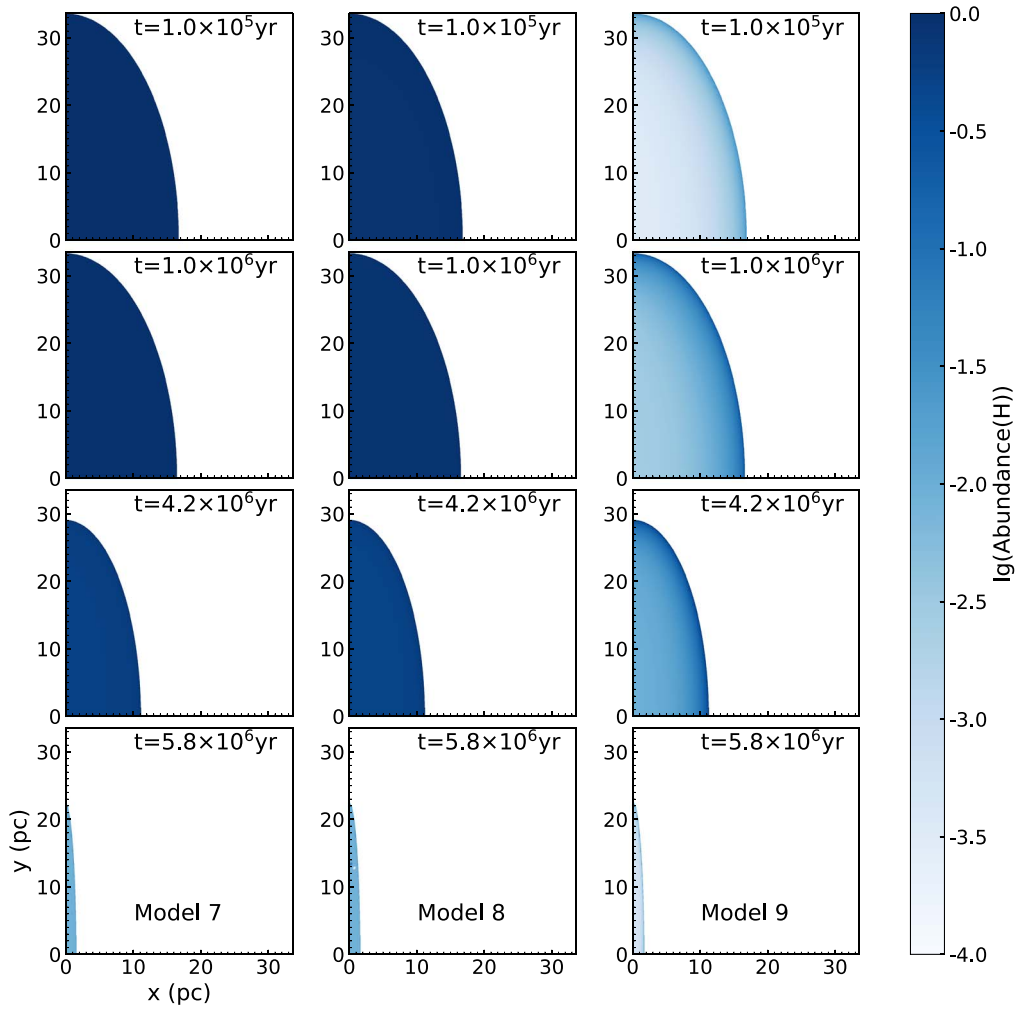


Figure A2. The H abundance distribution at different time in a gravitationally collapsing uniform prolate ellipsoidal cloud using models 7–9.

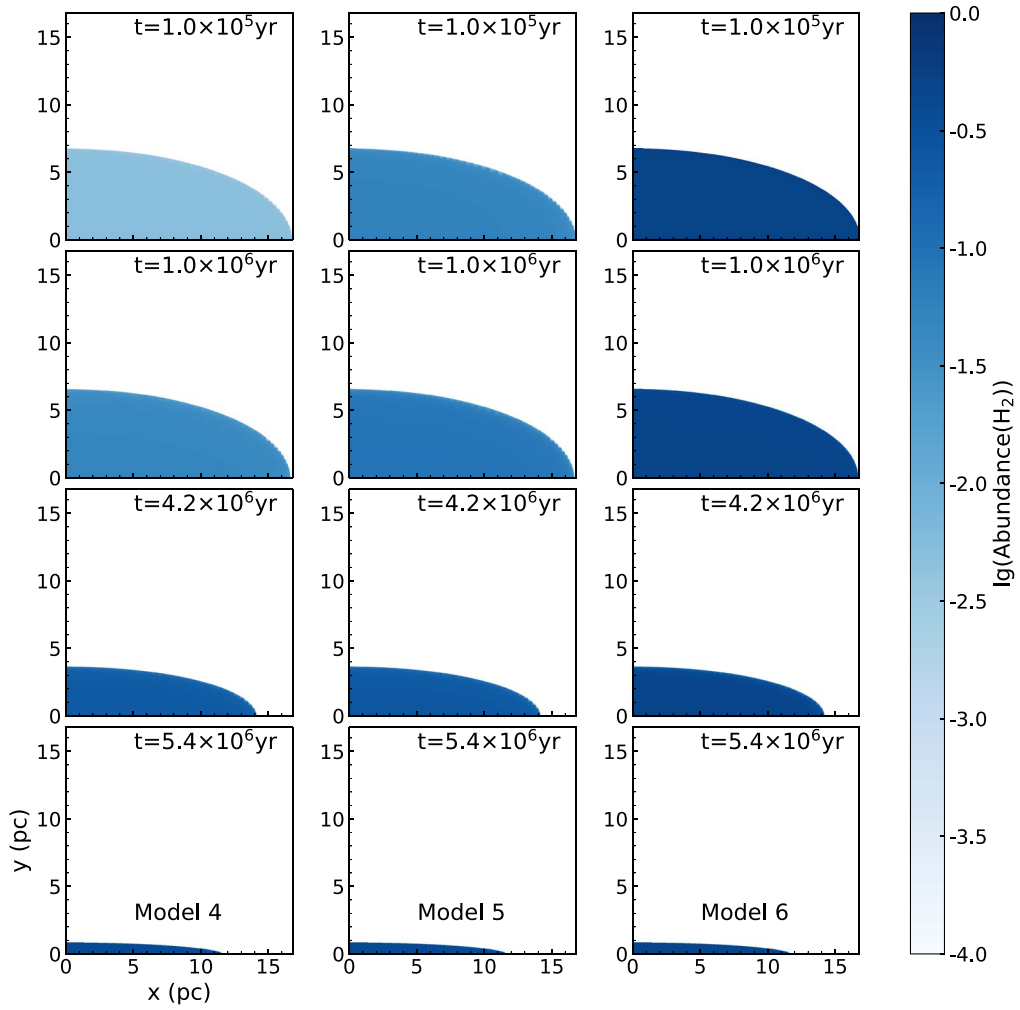


Figure A3. The H_2 abundance distribution at different time in models 4-6.

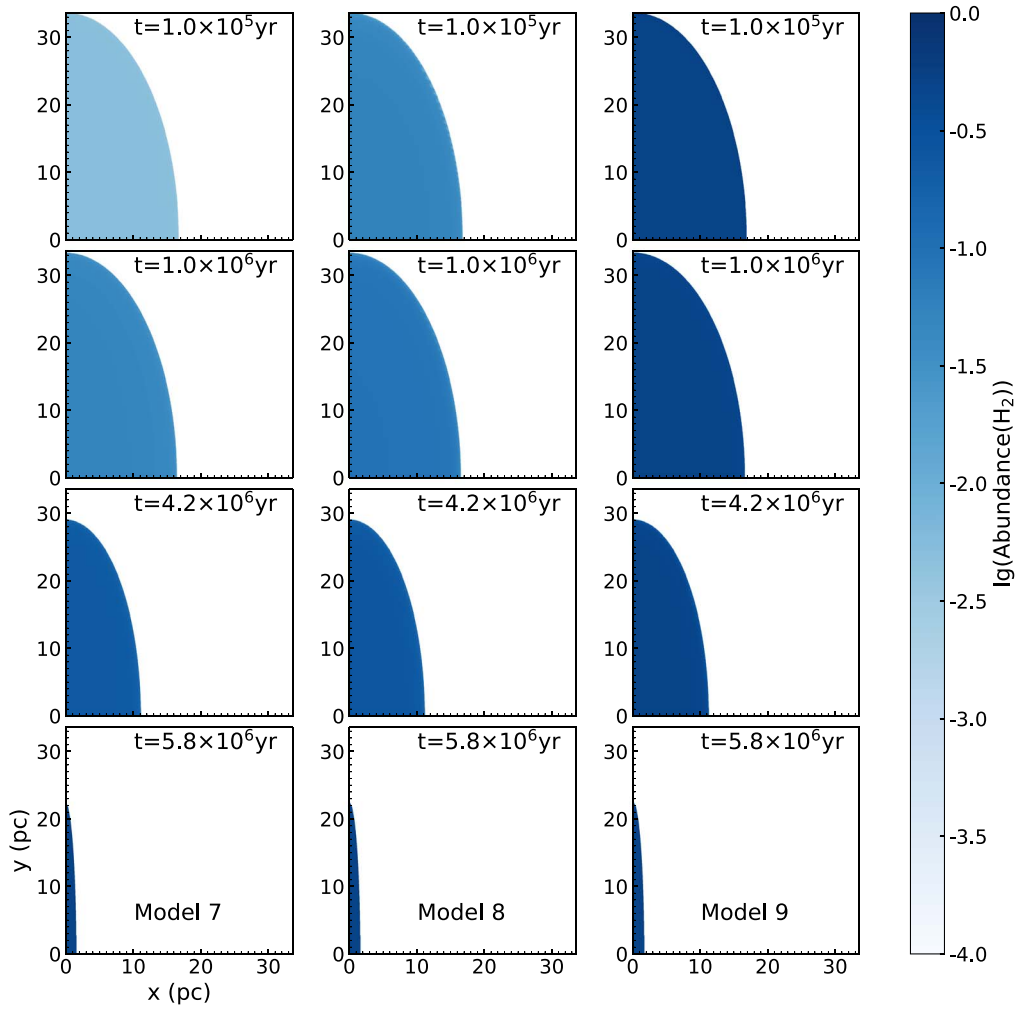


Figure A4. The H_2 abundance distribution at different time in models 7–9.

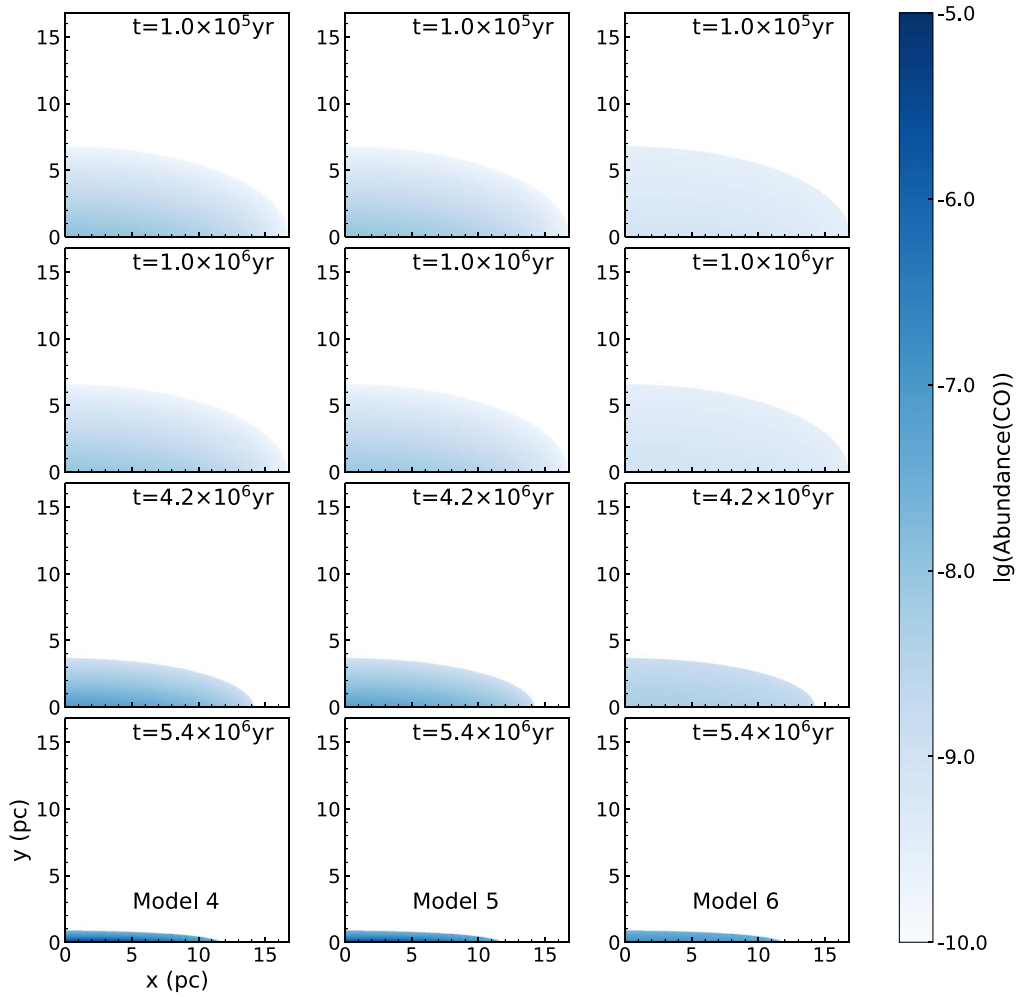


Figure A5. The CO abundance distribution at different time in models 4–6.

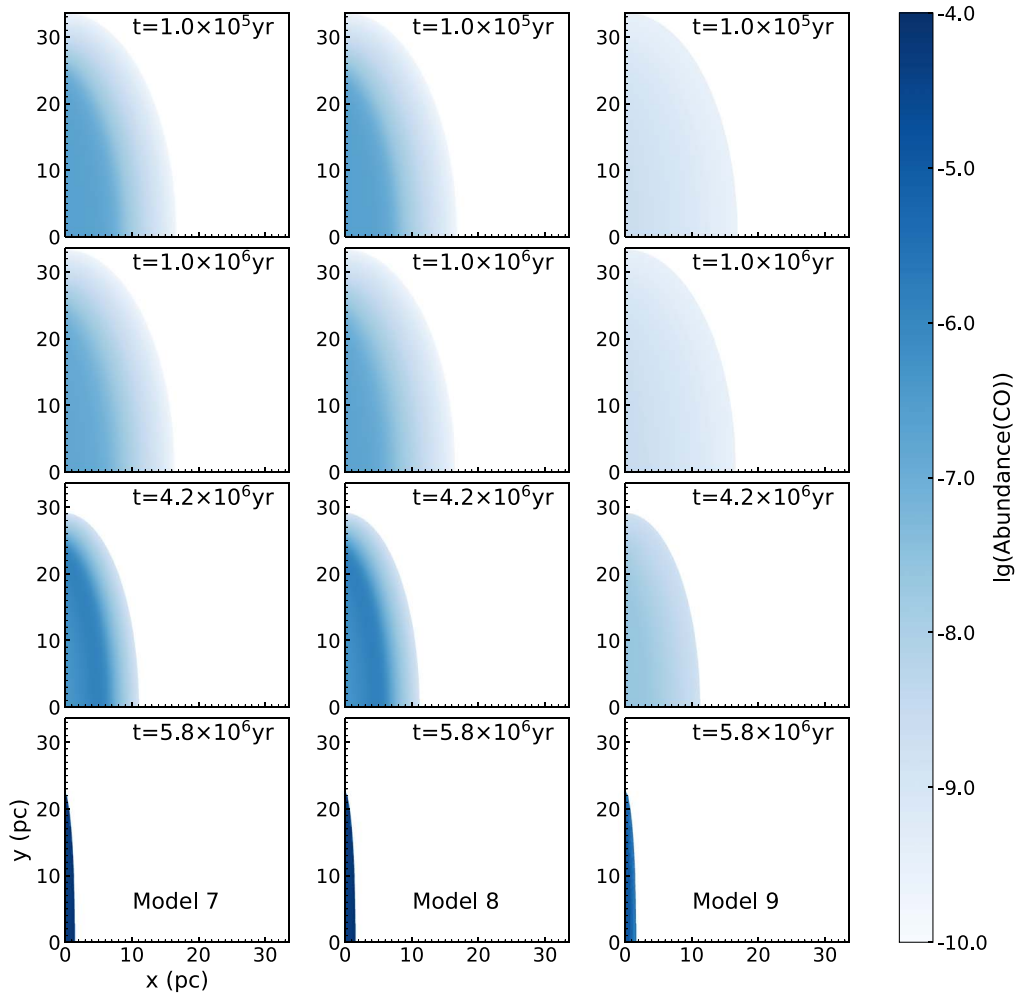


Figure A6. The CO abundance distribution at different time in models 7–9.

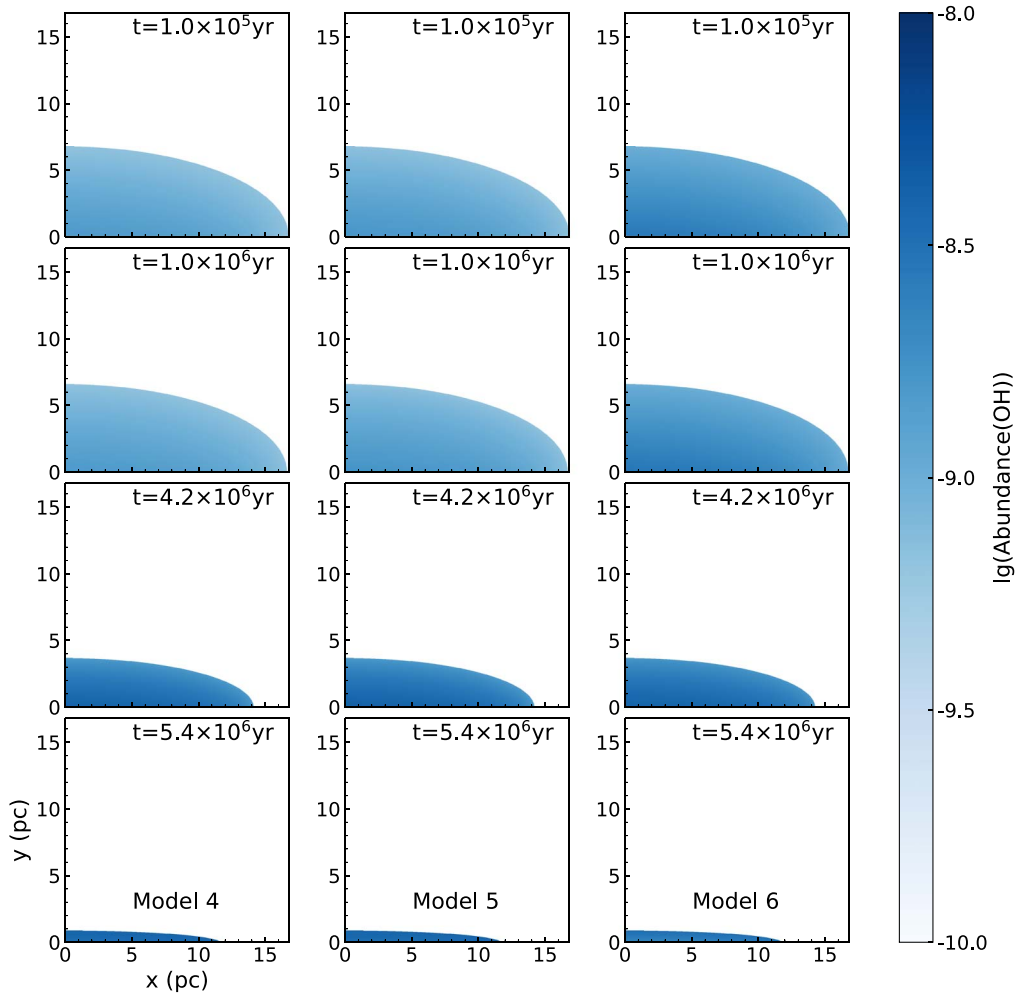


Figure A7. The OH abundance distribution at different time in models 4–6.

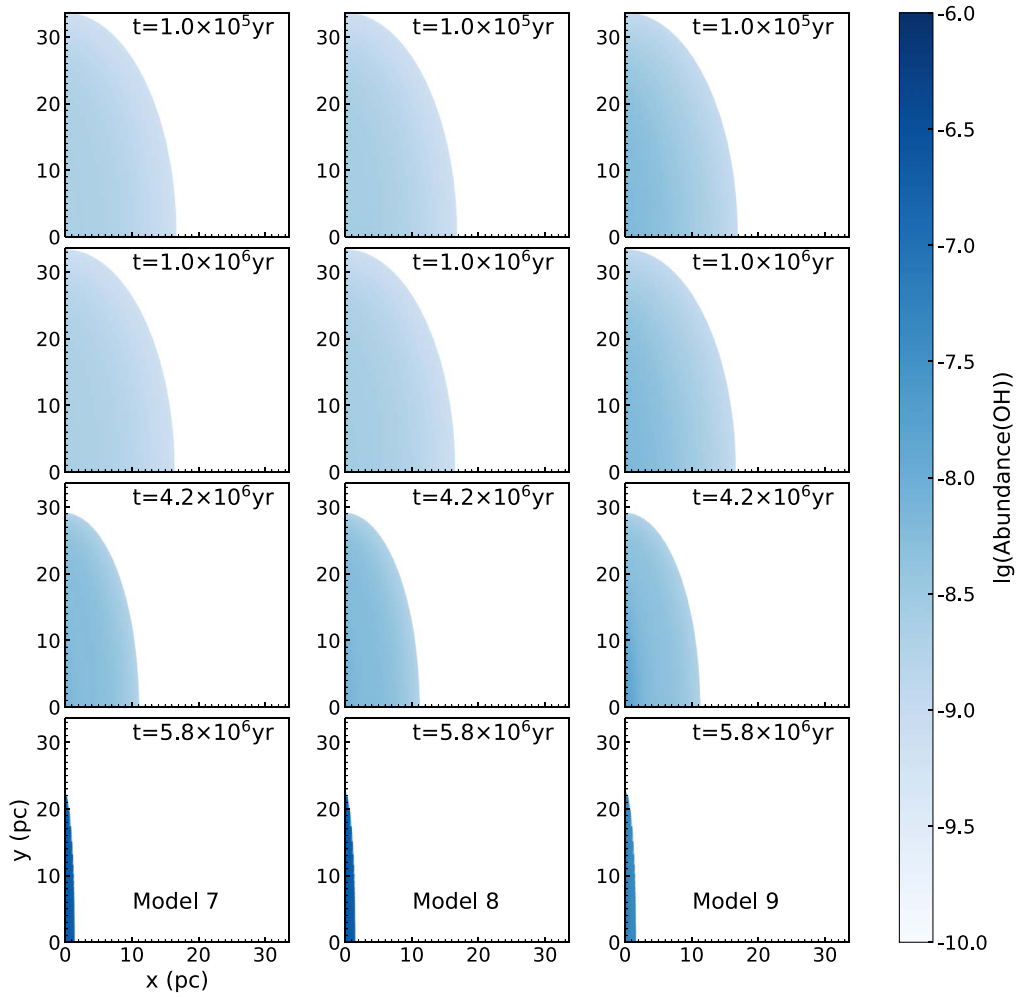


Figure A8. The OH abundance distribution at different time in models 7–9.

ORCID iDs

Fujun Du  <https://orcid.org/0000-0002-7489-0179>

References

- Balbus, S. A., & Hawley, J. F. 1991, *ApJ*, **376**, 214
- Ballesteros-Paredes, J., André, P., Hennebelle, P., et al. 2020, *SSRv*, **216**, 76
- Bania, T. M., & Lyon, J. G. 1980, *ApJ*, **239**, 173
- Barriault, L., Joncas, G., Falgarone, E., et al. 2010, *MNRAS*, **406**, 2713
- Bergin, E. A., & Tafalla, M. 2007, *ARA&A*, **45**, 339
- Bialy, S., & Sternberg, A. 2016, *ApJ*, **822**, 83
- Bianchi, S., Gonçalves, J., Albrecht, M., et al. 2003, *A&A*, **399**, L43
- Bigiel, F., Leroy, A., Walter, F., et al. 2008, *AJ*, **136**, 2846
- Bodenheimer, P., & Sweigart, A. 1968, *ApJ*, **152**, 515
- Bohlin, R. C., Savage, B. D., & Drake, J. F. 1978, *ApJ*, **224**, 132
- Burkhart, B., Lee, M.-Y., Murray, C. E., & Stanimirović, S. 2015, *ApJL*, **811**, L28
- Casoli, F., & Combes, F. 1982, *A&A*, **110**, 287
- Clark, P. C., Glover, S. C. O., Ragan, S. E., & Duarte-Cabral, A. 2019, *MNRAS*, **486**, 4622
- Crutcher, R. M. 1979, *ApJ*, **234**, 881
- Draine, B. T. 1978, *ApJS*, **36**, 959
- Draine, B. T., & Bertoldi, F. 1996, *ApJ*, **468**, 269
- Du, F. 2021, *RAA*, **21**, 077
- Du, F., & Bergin, E. A. 2014, *ApJ*, **792**, 2
- Ewen, H. I., & Purcell, E. M. 1951, *Natur*, **168**, 356
- Field, G. B. 1965, *ApJ*, **142**, 531
- Field, G. B., & Saslaw, W. C. 1965, *ApJ*, **142**, 568
- Field, G. B., Somerville, W. B., & Dressler, K. 1966, *ARA&A*, **4**, 207
- Fukui, Y., Mizuno, N., Yamaguchi, R., et al. 1999, *PASJ*, **51**, 745
- Garrod, R. T. 2013, *ApJ*, **765**, 60
- Garrod, R. T., & Pauly, T. 2011, *ApJ*, **735**, 15
- Geballe, T. R., & Oka, T. 2010, *ApJL*, **709**, L70
- Goldreich, P., & Lynden-Bell, D. 1965, *MNRAS*, **130**, 125
- Goldsmith, P. F., & Li, D. 2005, *ApJ*, **622**, 938
- Goldsmith, P. F., Li, D., & Krčo, M. 2007, *ApJ*, **654**, 273
- Grassi, T., Bovino, S., Schleicher, D. R. G., et al. 2014, *MNRAS*, **439**, 2386
- Grenier, I. A., Casandjian, J.-M., & Terrier, R. 2005, *Sci*, **307**, 1292
- Habing, H. J. 1968, BAN, **19**, 421
- Hartmann, L. 2003, *ApJ*, **585**, 398
- Hartmann, L., Ballesteros-Paredes, J., & Bergin, E. A. 2001, *ApJ*, **562**, 852
- Hartquist, T. W., Doyle, H. T., & Dalgarno, A. 1978, *A&A*, **68**, 65
- Hasegawa, T. I., Herbst, E., & Leung, C. M. 1992, *ApJS*, **82**, 167
- Holdship, J., Viti, S., Jiménez-Serra, I., Makrymallis, A., & Priestley, F. 2017, *AJ*, **154**, 38
- Indriolo, N., Blake, G. A., Goto, M., et al. 2010, *ApJ*, **724**, 1357
- Indriolo, N., & McCall, B. J. 2012, *ApJ*, **745**, 91
- Indriolo, N., Neufeld, D. A., Gerin, M., et al. 2015, *ApJ*, **800**, 40
- Kawamura, A., Mizuno, Y., Minamidani, T., et al. 2009, *ApJS*, **184**, 1
- Kramer, C., Richer, J., Mookerjee, B., Alves, J., & Lada, C. 2003, *A&A*, **399**, 1073
- Lada, E. A., & Blitz, L. 1988, *ApJL*, **326**, L69
- Langer, W. D., Velusamy, T., Pineda, J. L., Willacy, K., & Goldsmith, P. F. 2014, *A&A*, **561**, A122
- Langer, W. D., Velusamy, T., Pineda, J. L., et al. 2010, *A&A*, **521**, L17
- Le Bourlot, J., Pineau des Forets, G., Roueff, E., & Schilke, P. 1993, *ApJL*, **416**, L87
- Lee, H. H., Herbst, E., Pineau des Forets, G., Roueff, E., & Le Bourlot, J. 1996, *A&A*, **311**, 690
- Lee, M.-Y., Stanimirović, S., Douglas, K. A., et al. 2012, *ApJ*, **748**, 75
- Li, D., & Goldsmith, P. F. 2003, *ApJ*, **585**, 823
- Li, D., Tang, N., Nguyen, H., et al. 2018, *ApJS*, **235**, 1
- Li, D., Xu, D., Heiles, C., Pan, Z., & Tang, N. 2015, *PKAS*, **30**, 75
- Lin, C. C., Mestel, L., & Shu, F. H. 1965, *ApJ*, **142**, 1431
- Liszt, H., & Lucas, R. 1996, *A&A*, **314**, 917
- Maret, S., & Bergin, E. A. 2015, *Astrochem: Abundances of Chemical Species in the Interstellar Medium*, ascl:1507.010
- McCall, B. J., Geballe, T. R., Hinkle, K. H., & Oka, T. 1999, *ApJ*, **522**, 338
- McCrea, W. H., & McNally, D. 1960, *MNRAS*, **121**, 238
- McDowell, M. R. C. 1961, *Obs*, **81**, 240
- McElroy, D., Walsh, C., Markwick, A. J., et al. 2013, *A&A*, **550**, A36
- Morris, M., & Jura, M. 1983, *ApJ*, **264**, 546
- Mouschovias, T. C., Tassis, K., & Kunz, M. W. 2006, *ApJ*, **646**, 1043
- Oort, J. H. 1954, BAN, **12**, 177
- Padovani, M., Ivlev, A. V., Galli, D., & Caselli, P. 2018, *A&A*, **614**, A111
- Parker, E. N. 1966, *ApJ*, **145**, 811
- Pineau des Forets, G., Roueff, E., & Flower, D. R. 1992, *MNRAS*, **258**, 45P
- Pineda, J. L., Langer, W. D., Velusamy, T., & Goldsmith, P. F. 2013, *A&A*, **554**, A103
- Planck Collaboration, Ade, P. A. R., Aghanim, N., et al. 2011, *A&A*, **536**, A19
- Reach, W. T., Koo, B.-C., & Heiles, C. 1994, *ApJ*, **429**, 672
- Ruud, M., Wakelam, V., & Hersant, F. 2016, *MNRAS*, **459**, 3756
- Schinnerer, E., Meidt, S. E., Pety, J., et al. 2013, *ApJ*, **779**, 42
- Schnee, S., & Goodman, A. 2005, *ApJ*, **624**, 254
- Seifried, D., Beuther, H., Walch, S., et al. 2022, *MNRAS*, **512**, 4765
- Shaw, G., Ferland, G. J., Srianand, R., et al. 2008, *ApJ*, **675**, 405
- Shu, F. H. 1977, *ApJ*, **214**, 488
- Sofia, U. J., Lauroesch, J. T., Meyer, D. M., & Cartledge, S. I. B. 2004, *ApJ*, **605**, 272
- Stanimirović, S., Murray, C. E., Lee, M.-Y., Heiles, C., & Miller, J. 2014, *ApJ*, **793**, 132
- Sternberg, A., Le Petit, F., Roueff, E., & Le Bourlot, J. 2014, *ApJ*, **790**, 10
- Tang, N., Li, D., Heiles, C. E. & ISM Group in National Astronomical Observatories, C. 2017, *AAS Meeting Abstracts*, 229, 311.02
- Tang, N., Li, D., Yue, N., et al. 2021, *ApJS*, **252**, 1
- Tielens, A. G. G. M. 2010, *The Physics and Chemistry of the Interstellar Medium* (Cambridge: Cambridge Univ. Press)
- Tielens, A. G. G. M., & Hollenbach, D. 1985, *ApJ*, **291**, 722
- Umebayashi, T., & Nakano, T. 1981, *PASJ*, **33**, 617
- van der Tak, F. F. S., & van Dishoeck, E. F. 2000, *A&A*, **358**, L79
- Vázquez-Semadeni, E., Ballesteros-Paredes, J., & Klessen, R. S. 2003, *ApJL*, **585**, L131
- Wakelam, V., Herbst, E., Loison, J. C., et al. 2012, *ApJS*, **199**, 21
- Wannier, P. G., Lichten, S. M., & Morris, M. 1983, *ApJ*, **268**, 727
- Ward-Thompson, D., André, P., & Kirk, J. M. 2002, *MNRAS*, **329**, 257
- Weselak, T., Galazutdinov, G. A., Beletsky, Y., & Krelowski, J. 2010, *MNRAS*, **402**, 1991
- Wolfire, M. G., McKee, C. F., Hollenbach, D., & Tielens, A. G. G. M. 2003, *ApJ*, **587**, 278